



Neutrino Mass Constraints from Reconstructing the Large-scale Structure: Systematic Uncertainty

Chok Lap Chung¹, Derek Inman² , Xin Wang^{1,3} , Erhao Shang¹, Zi Zhuang¹, Fucheng Yuan¹, and Ue-Li Pen^{4,5,6,7,8} 

¹School of Physics and Astronomy, Sun Yat-Sen University, Zhuhai 5109082, China; wangxin35@mail.sysu.edu.cn

²Kavli IPMU (WPI), UTIAS, The University of Tokyo, Kashiwa, Chiba 277-8583, Japan

³CSST Science Center for the Guangdong-Hong Kong-Macau Greater Bay Area, SYSU, China

⁴Institute of Astronomy and Astrophysics, Academia Sinica, 645 N Aohoku Pl, Hilo, HI 96720, USA

⁵Canadian Institute for Theoretical Astrophysics, 60 St. George Street, Toronto, ON M5S 3H8, Canada

⁶Canadian Institute for Advanced Research, 180 Dundas St West, Toronto, ON M5G 1Z8, Canada

⁷Dunlap Institute for Astronomy and Astrophysics, University of Toronto, 50 St George Street, Toronto, ON M5S 3H4, Canada

⁸Perimeter Institute of Theoretical Physics, 31 Caroline Street North, Waterloo, ON N2L 2Y5, Canada

Received 2022 November 24; revised 2023 March 17; accepted 2023 March 20; published 2023 May 17

Abstract

We examine the possibility of applying the baryonic acoustic oscillation reconstruction method to improve the neutrino mass Σm_ν constraint. Thanks to the Gaussianization of the process, we demonstrate that the reconstruction algorithm could improve the measurement accuracy by roughly a factor of two. On the other hand, the reconstruction process itself becomes a source of systematic error. While the algorithm is supposed to produce the displacement field from a density distribution, various approximations cause the reconstructed output to deviate on intermediate scales. Nevertheless, it is still possible to benefit from this Gaussianized field, given that we can carefully calibrate the “transfer function” between the reconstruction output and theoretical displacement divergence from simulations. The limitation of this approach is then set by the numerical stability of this transfer function. With an ensemble of simulations, we show that such systematic error could become comparable to statistical uncertainties for a DESI-like survey and be safely neglected for other less ambitious surveys.

Key words: (cosmology:) large-scale structure of universe – cosmology: observations – neutrinos

1. Introduction

The large-scale structure (LSS) contains valuable information about the evolution of our universe, extractable from the statistical measurement of galaxy surveys. Increasingly precise LSS studies have the potential to discover new physical results such as dark energy (Tegmark et al. 2006; Alam et al. 2017), cosmic neutrinos (Lesgourgues & Pastor 2006; Riemer-Sørensen et al. 2013; Palanque-Deslauriers et al. 2020) or modified gravity (Giannantonio et al. 2010; Li & Zhao 2019). For example, in the two-point statistics, these effects manifested either as distinctive features or broadband shape change. Due to its robust constraining power, the baryonic acoustic oscillation (BAO) (Peebles & Yu 1970; Sunyaev & Zeldovich 1970; Bond & Efstathiou 1987; Hu & Sugiyama 1996; Eisenstein 2002; Blake & Glazebrook 2003; Hu & Haiman 2003; Seo & Eisenstein 2003) is probably one of the most significant feature in LSS measurement. Other examples include some possible primordial features from different scenarios of inflation models (Chen et al. 2016). On the other hand, the broadband full shape of the power spectrum is affected by more complicated physics, including nonlinear clustering bias (Desjacques et al. 2018), baryonic feedback (Jing et al. 2006; Rudd et al. 2008), massive neutrinos

(Lesgourgues & Pastor 2006) and alternative gravity theories (Clifton et al. 2012). Consequently, statistical constraints with full-shape two-point statistics usually plateau at quasi-linear scales as the modeling becomes complicated due to the nonlinear structure formation and information leakage into higher-order statistics (Rimes & Hamilton 2005, 2006).

Unsurprisingly, various techniques have been developed to maximize information content diminished by the nonlinear structure formation. For example, Eisenstein et al. (2007) introduced a reconstruction algorithm that partially reverses the BAO broadening and improves the accuracy of dark energy measurement. Along this direction, recent developments in iterative reconstruction have further sharpened the BAO peak and recovered the linear BAO signature, including the *isobaric reconstruction* (Pan et al. 2017; Wang et al. 2017; Yu et al. 2017; Zhu et al. 2017, 2018) and other similar techniques as well (Schmittfull et al. 2017; Hada & Eisenstein 2018; Shi et al. 2018). Meanwhile, forward modeling reconstruction has also been successfully implemented and achieved a similar level of improvement (Kitaura & EnBlin 2008; Seljak et al. 2017; Schmidt et al. 2019). Particularly for the backward reconstruction, their accomplishment relies on two main changes brought to the density field. The first is the recovery

of the primordial signal itself (see Li et al. (2021) for the reconstruction of other inflationary signatures), which is achieved by solving the continuity equation for the displacement field. Moreover, the reconstructed field is also more Gaussian so that most information is encoded in the two-point statistics (Pan et al. 2016). Hence, even though these reconstruction algorithms were initially developed for BAO purposes, they should also be beneficial to physical effects that affect the broadband shape of the power spectrum, e.g., neutrino and modified gravity. As a concrete example, we consider whether reconstruction can improve measurements of the neutrino mass. Neutrinos are a form of hot dark matter, and their large thermal motions lead to a scale-dependent suppression in the matter power spectrum which can be used to constrain their masses (Lesgourgues & Pastor 2006; Ivanov et al. 2020).

To date, the broadband power change of these reconstruction methods has yet to be thoroughly investigated. One crucial challenge is the model accuracy of the reconstructed field. Unlike the BAO signal, which is quite resilient against deformation of the power spectrum, the shape itself could easily be affected by any k -dependent effects and this is indeed what happens to the isobaric reconstruction. Even though, in principle, the algorithm should recover the displacement divergence, a straightforward test shows a notable difference at both the field and statistical levels. The underlying reason is that the algorithm makes several assumptions for the mass conservation equation to be solvable (Wang & Pen 2019). Still, a Gaussianized field estimator is just too attractive to be ignored. One possible workaround is carefully calibrating a “transfer function” between the reconstructed field and the actual displacement. As long as the calibration is stable, which means it is not “randomly” affected by numerical or other observational effects, we can persuade ourselves to trust the result.

In this paper, we examine this type of systematic error quantitatively. Of course, the list of possible random sources will be lengthy. As the first step, we will only inspect the reconstruction error caused by the random fields, i.e., random seeds in simulations. The paper is organized in the following: in Section 2, we discuss the Gaussianization aspect of the isobaric reconstruction method; in Section 3, we then estimate the numerical instability, i.e., the reconstruction systematics; and finally, we discuss the consequences for future neutrino constraints with LSS and conclude in Section 4.

2. Isobaric Reconstruction as a Gaussianization Procedure

Gaussianization has historically been an active goal of many LSS studies. For example, a logarithmic transformation or local Gaussianization procedure seems to reverse the non-Gaussian evolution (Weinberg 1992; Neyrinck 2011). However, these

methods only changed the one-point probability density function (PDF), and did not reverse any structure formation process. On the other hand, the isobaric reconstruction, and other similar techniques, could also be viewed as a Gaussianization procedure. This is achieved by solving the *nonlinear* mass conservation equation

$$\det\left(\frac{\partial x_i}{\partial q_j}\right) = \det(\delta_{ij}^K + \partial_{ij}^2\phi) = \frac{\rho_{\text{init}}}{\rho} = \frac{1}{1 + \delta_\rho}. \quad (1)$$

Here \mathbf{q} and \mathbf{x} are Lagrangian and Eulerian coordinates of particles respectively, and the displacement vector and potential are defined as $\Psi(\mathbf{q}) = \mathbf{x} - \mathbf{q} = \nabla\phi(\mathbf{q})$, where δ_{ij}^K is the Kronecker delta. By solving Equation (1), the reconstruction algorithm eliminates this nonlinear coordinate transformation and produces the reconstructed ϕ_{rec} field on a grid that is close to the Lagrangian frame. Hereafter, we will denote the reconstructed field as $\delta_{\text{rec}} = \nabla^2\phi_{\text{rec}}$ and displacement divergence as $\delta_{\text{disp}} = \nabla \cdot \Psi$.

The frameshift from Euler to Lagrangian is the reason behind the BAO sharpening in the correlation function, making it more precise to identify the sound horizon scale at $s \approx 100$ Mpc/h via the peak location. Nevertheless, this is not the only improvement the reconstruction algorithm has brought. As shown in the upper panel of Figure 1, this reconstructed field is very close to Gaussian compared to the log-normal distribution of density ρ . In the *lower* panel, we also compare the normalized covariance matrix of the power spectrum $P(k)$ (also in Pan et al. 2016; Wang et al. 2017). As shown, before the BAO scale where $k \lesssim 0.5$ h/Mpc, the covariance matrix is very close to diagonal. This means that the reconstruction method could serve as a Gaussianization process and reverse the information leakage from the initial Gaussian field to higher-order statistics.

Consequently, the reconstruction can indeed improve the measurement accuracy of broadband physics like the neutrino mass Σm_ν . To see this, we could examine the information gain with the Fisher matrix, which is defined as

$$F_{ij} = \sum_{\alpha,\beta} \frac{\partial P(k_\alpha)}{\partial p_i} C_{\alpha\beta}^{-1} \frac{\partial P(k_\beta)}{\partial p_j}, \quad (2)$$

where $C_{\alpha\beta}$ is the covariance matrix. To start, we consider the idealized case of a shot-noiseless survey, so that the diagonal terms of the non-Gaussian covariance matrix were rescaled to coincide with the Gaussian contribution. Without presenting more details, which will be shown later in Section 4, we plot the one- σ cosmological constraints on $M_\nu = \Sigma m_\nu$ in Figure 2. As demonstrated, for both fiducial masses ($M_\nu = 3 \times 100$ and 3×50 meV), the final constraints improve by roughly a factor of two. Here we assume a survey with volume $V = 10$ (Gpc/h)³. This sets the most ideal baseline for potential improvement using reconstruction.

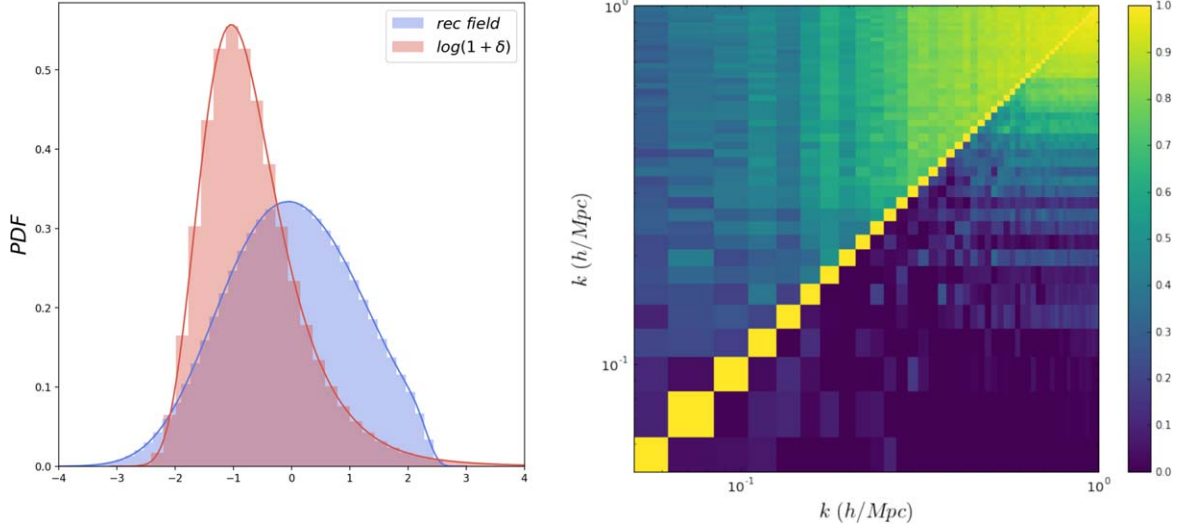


Figure 1. Isobaric reconstruction serves as a Gaussianization procedure. Left panel shows the one-point PDF of the reconstructed field (blue) $\nabla^2\phi$ and the logarithm of matter density field (red). Right panel compares the normalized covariance matrices ($\bar{C}_{\alpha\beta} = C_{\alpha\beta} / \sqrt{C_{\alpha\alpha} C_{\beta\beta}}$) of the power spectrum $P(k_\alpha)$ of density (upper triangle) and reconstructed field (lower triangle) at redshift $z = 0$. This is a re-plot of Figure 1 from Pan et al. (2016). Around the quasi-linear scales, the off-diagonal elements of the reconstructed field are significantly lower than those of density field.

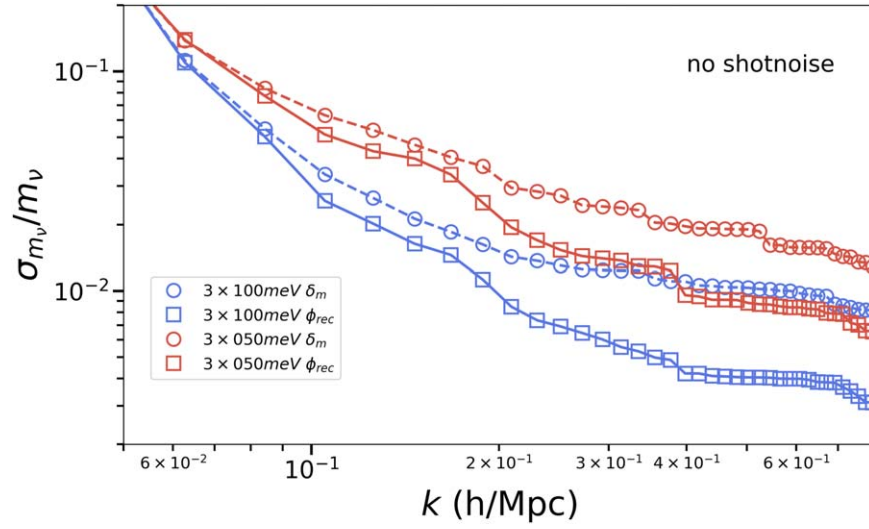


Figure 2. One- σ constraints of an idealized shot-noiseless survey on Σm_ν , as a function of maximum k , assuming survey volume $V = 10$ (Gpc/h) 3 . The square-solid-line signifies the reconstructed field ϕ_{rec} whereas circle-dashed-line is the constraints with matter density δ itself. Due to Gaussianization of the field, even though the signal in $P(k)$ decreases after the reconstruction, the final constraints still improve by roughly a factor of two.

3. Systematics Analysis of the Broadband Shape

Of course, the conclusion above does not consider various practical complications. Among everything else, the most crucial caveat is that the algorithm does not produce the actual displacement field. As discussed in Wang & Pen (2019), the discrepancy between δ_{rec} and δ_{disp} is caused by three approximations made by the reconstruction algorithm: (1) no shell-crossing; (2) Ψ contains no transverse component; and (3) negligible initial fluctuation, i.e., $\delta_{\text{init}} \approx 0$. All of them break

down at some point, which means that while an accurate theoretical model might still be possible, it will surely be very challenging to get. Moreover, the clustering bias further complicates the situation. From the density matching introduced by Wang & Pen (2019), the bias could affect the reconstruction in two significant ways. One is the coordinate shift $\Delta\xi^9$, and the other is the modified kernel in the perturbative expansion of the

⁹ $\Delta\xi = \xi - q$, where ξ is the reconstructed isobaric frame and q is the Lagrangian coordinates.

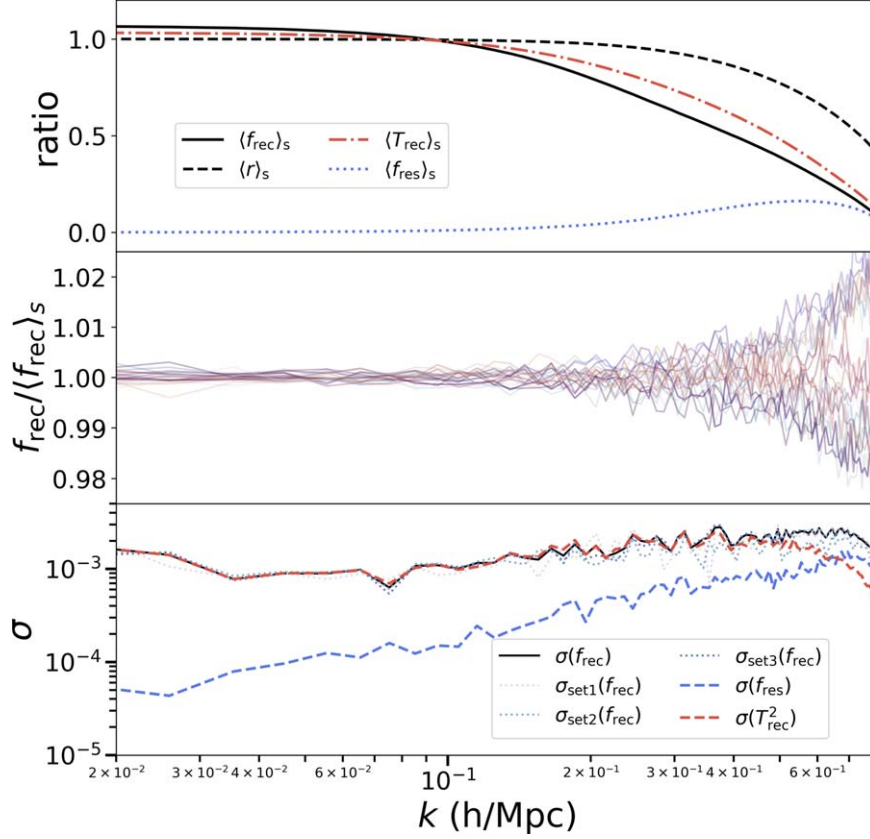


Figure 3. Power spectrum comparison of reconstructed field and true displacement divergence, obtained from 20 simulations with $V = 1(\text{Gpc}/h)^3$ and $n_{\text{particle}} = 512^3$. Here $\langle \dots \rangle_s$ denotes average among all simulations. Upper panel shows various ratios averaged with 20 simulations; the middle panel demonstrates the fluctuation among these 20 simulations and finally the lower panel presents the standard deviation. In the lower panel, we can see that the variance is dominated by the randomness of transfer function $T^2(k)$ at most of the scales. To verify the systematic nature of the variation, we divide our simulations into three subsets (*set1*, *set2* and *set3*) with a quarter, half and three-quarters of the total simulations.

displacement. The severity of the two effects is different, the frameshift will cause additional smearing of BAO signal and the modified kernel (with unknown bias parameters) will change the shape of the power spectrum.

For BAO applications or other primordial features (Li et al. 2021), these assumptions do not pose a serious challenge as they are usually quite robust. On the other hand, however, for the broadband feature like the neutrino mass, any k -dependent modification could be crucial. In the first panel of Figure 3, we plot the ratio of power spectrum between reconstructed field and the real displacement as the black-solid line

$$f_{\text{rec}}(k) = \frac{P_{\text{rec}}}{P_{\text{disp}}}(k). \quad (3)$$

Besides the small-scale deviation, we can also identify a large-scale bias of a few percent at low k . The reason behind this deviation is beyond the scope of this paper, but recent theoretical studies, e.g., Ota et al. (2021), also point out similar differences for other reconstruction methods.

At first glance, such deviation does seem to discourage us from using a reconstructed broadband power spectrum for any cosmological measurement. It is noticeable that the reconstructed ratio $f_{\text{rec}}(k)$ is much further from unity than the cross coefficient (black-dashed line),

$$r_{\text{rec}}(k) = \frac{P_{\text{rec} \times \text{disp}}}{\sqrt{P_{\text{rec}} P_{\text{disp}}}}, \quad (4)$$

which characterizes the residual BAO peak smearing and is very close to one until wavenumber $k \lesssim 0.5 \text{ h/Mpc}$. Here, $P_{\text{rec} \times \text{disp}}$ is the cross-correlation between reconstructed and displacement divergence field. Nevertheless, as discussed in the Introduction, as long as we can numerically calibrate the model with simulation, it is hard to resist the potential accuracy improvement shown in Figure 2.

To understand these curves in Figure 3, we can decompose the reconstructed field as

$$\delta_{\text{rec}}(\mathbf{k}) = T_{\text{rec}}(k) \delta_{\text{disp}}(\mathbf{k}) + \delta_{\text{res}}(\mathbf{k}). \quad (5)$$

Here $T(k)$ is a deterministic transfer function describing the deviation from the real displacement field, which we assume to be isotropic. $\delta_{\text{res}}(\mathbf{k})$ is some random residual that does not correlate with $\delta_{\text{disp}}(\mathbf{k})$. To “predict” the power spectrum shape of $\delta_{\text{rec}}(\mathbf{k})$, we are interested in the ratio between the power spectrum of $\delta_{\text{rec}}(\mathbf{k})$ and that of the displacement field

$$f_{\text{rec}}(k) = \frac{P_{\text{rec}}}{P_{\text{disp}}} = T_{\text{rec}}^2 + f_{\text{res}}, \quad (6)$$

where $f_{\text{res}} = P_{\text{res}}/P_{\text{disp}}$ and P_{res} is the auto power spectrum of δ_{res} .

To investigate the numerical stability of the reconstruction, we ran 20 cold dark matter (CDM)-only simulations ($V = 1 \text{ (Gpc/h)}^3$, $n_{\text{particle}} = 512^3$) with different initial conditions. In the *upper* panel of Figure 3, we show various ratios just defined. Here $\langle \dots \rangle_s$ denotes the average among these simulations. To understand the difference between f_{rec} (or equivalently T_{rec}) and r_{rec} , we could express the cross-coefficient $r_{\text{rec}}(k)$ with the decomposition (5), i.e., $r_{\text{rec}}(k) = P_{\text{rec} \times \text{disp}} / \sqrt{P_{\text{rec}} P_{\text{disp}}} = T_{\text{rec}} / \sqrt{T_{\text{rec}}^2 + f_{\text{res}}}$. More conveniently, we have

$$T_{\text{rec}}(k) = r_{\text{rec}}(k) \sqrt{\frac{f_{\text{res}}}{1 - r_{\text{rec}}^2}}. \quad (7)$$

Hence, only if the ratio $f_{\text{res}}/(1 - r_{\text{rec}}^2)$ equals one (i.e., $f_{\text{res}} \rightarrow 0$) would we have $T_{\text{rec}} = r_{\text{rec}}$. In reality, however, the residual power fraction f_{res} only has a small bump at high- k (dotted-blue line of the upper panel in Figure 3), whereas $1 - r_{\text{rec}}^2$ approaches unity. Consequently, $f_{\text{res}}/(1 - r_{\text{rec}}^2)$ becomes less than unity around $k \gtrsim 0.1$. In other words, T_{rec} will always drop faster than r_{rec} at high- k . For cosmological measurements, we are mostly interested in the power spectrum ratio f_{rec} (Equation (6)). As mentioned previously, even though it is desirable to understand technical details behind these curves, we do not need to achieve this with, e.g., the perturbation theory. As long as we are able to accurately calibrate $T_{\text{rec}}(k)$ from simulations, it could be applied to cosmological constraints.

However, there is at least one more systematic we still need to consider. Due to the numerical nature of the reconstruction algorithm, the calibrated transfer function T_{rec} also has uncertainties, which serve as the systematic error limiting the measurement. In the *middle* panel of Figure 3, we demonstrate the fractional variations $f_{\text{rec}}/\langle f_{\text{rec}} \rangle_s$ among our simulation set. In the *lower* panel, we calculate the standard deviation of different components from our limited simulation set. From the figure, the one-sigma variation of f_{rec} is around a few times 10^{-3} (black-solid line). As systematic errors, this variation does not diminish as the number of samples increase. To test, we divide our simulations into three subsets (*set1*, *set2* and *set3*) with a quarter, half and three-quarters of the total simulations. As we can see (dotted line), the variations of these samples are very

similar to each other, suggesting they are indeed systematic errors. From Equation (6), the variation $\sigma(f_{\text{rec}})$ has two contributions, $\sigma(T_{\text{rec}}^2)$ and $\sigma(f_{\text{res}})$ respectively. From our measurement, the transfer function dominates the variation (red-solid line versus blue-dashed line) until $k \sim 0.6 \text{ h/Mpc}$.

4. Consequences for Neutrino Mass Measurement

After quantifying the intrinsic variance induced by the reconstruction algorithm, we are ready to investigate its consequences and compare it with statistical uncertainties. To start, we need to determine how the reconstruction algorithm performs in the presence of cosmic neutrinos. We run cosmological N -body simulations evolving both CDM and neutrinos, using the CUBEP³M code (Harnois-Déraps et al. 2013) modified to include the neutrinos as a separate particle species (Inman et al. 2015). Each simulation contains $N_c = 768^3$ CDM particles and $N_\nu = 768^3$ neutrino particles within a box of side length $L = 600 \text{ Mpc/h}$. We consider two fiducial neutrino masses: $3 \times 50 \text{ meV}$ and $3 \times 100 \text{ meV}$. The energy density of the neutrinos is $\Omega_\nu = M_\nu/93.14h^2$ (Mangano et al. 2005), while other cosmological parameters are consistent with *Planck*: $\Omega_{cb} = 0.32$, $n_s = 0.96$ (Planck Collaboration et al. 2020). In the CUBEP³M neutrino implementation, neutrinos are started at a later redshift ($z = 10$) than CDM ($z = 100$). The value of σ_8 is specified at the initial neutrino redshift and is $\sigma_8(M_\nu = 3 \times 100 \text{ meV}) = 0.09$, $\sigma_8(M_\nu = 3 \times 50 \text{ meV}) = 0.0927$ and $\sigma_8(M_\nu = 0 \text{ meV}) = 0.095$. We have also run a simulation without cosmological neutrinos where we keep Ω_{cb} fixed. Keeping Ω_{cb} fixed instead of $\Omega_m = \Omega_{cb} + \Omega_\nu$ ensures that the CDM phases are the same between simulations (Bayer et al. 2022), and should better isolate the effect of reconstruction. We furthermore use the same method to generate CDM perturbations (e.g., using $z = 10$ transfer functions propagated back to $z = 100$). When applying the isobaric reconstruction, we use the CDM density field only, as this is what most correlates with halos (Brandbyge et al. 2010; Villaescusa-Navarro et al. 2013). Moreover, to calculate the variation of the power spectrum with respect to neutrino masses (Equation (2)), we also run simulations where we vary neutrino mass by $\pm 0.0025 \text{ meV}$ for $M_\nu = 3 \times 50 \text{ meV}$ and $\pm 0.005 \text{ meV}$ for $M_\nu = 3 \times 100 \text{ meV}$, and also adjust σ_8 consistently. We have run seven simulations with the above settings in total, all using the same random seed for the initial condition.

For the baseline result shown in Figure 2, we consider an idealized survey without shot noise, so that the diagonal terms of the non-Gaussian covariance matrix can be rescaled to coincide with the Gaussian contribution

$$C_{\alpha\beta} = C_{\alpha\beta}^G = \frac{2k_F^3}{V_s(k)} P(k_\alpha) P(k_\beta), \quad (8)$$

where $V_s = 4\pi k^2 \Delta k$ is the volume of spherical surface in Fourier space, and k_F is the fundamental mode of the box,

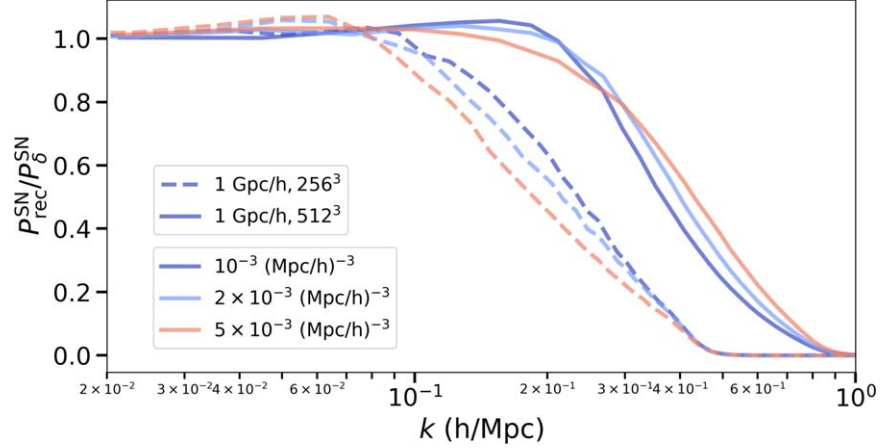


Figure 4. Numerical test on how reconstruction affects the shot noise contribution. Various curves show the ratio of power spectra $f^{\text{SN}}(k)$ (Equation (13)) between the post- and pre-reconstruction shot noise fields (Equations (11) and (12)). Different colors signify different number densities of the subsampled fields. As shown, the reconstruction slightly increases the shot noise power before reducing it to zero at high- k . This damping is mainly caused by the internal smoothing of the reconstruction algorithm. As shown, the damping scales of our higher-resolution maps (512^3 , solid lines) are much smaller than those of the lower-resolution maps (256^3 , dashed lines).

$k_F = 2\pi/L$, with L being the box size of the simulation. Here we assume the survey volume $V = 10 \text{ (Gpc/h)}^3$. For both fiducial masses, the final constraints improve by roughly a factor of two. This sets the ideal baseline for potential improvement in measuring the neutrino mass with reconstruction.

Given the intrinsic variation of the reconstruction method, we would like to understand further how this uncertainty propagates to cosmological constraints. Following the standard approach (Huterer & Takada 2005; Huterer et al. 2006), we define the bias on parameter p_i as

$$\delta_{\text{sys}}(\hat{p}_i) = (F^{-1})_{ij} B_j, \quad (9)$$

where F_{ij} is the Fisher matrix, and the bias vector B_j is given by

$$B_j = \sum_{\alpha} \delta P_{\text{sys}}(k_{\alpha}) C_{\alpha\beta}^{-1} \frac{\partial P(k_{\beta})}{\partial p_j}, \quad (10)$$

where δP_{sys} is the systematic deviation of the power spectrum. As demonstrated in the last section, our systematic error is multiplicative, therefore we have $\delta P_{\text{sys}}/P_{\text{rec}} = \sigma(f_{\text{rec}})$.

For a more realistic description of the LSS survey, we will include both clustering bias and shot noise in the covariance matrix, including both the on- and off-diagonal terms. However, instead of estimating the covariance matrix from the reconstructed halo samples, given the high numerical cost, we assume that the algorithm does not significantly change the shot noise. We test this ansatz by subsampling the dark matter particles and evaluating the shot noise before and after the reconstruction. Specifically, for a given simulation, we subsample particles to a particular number density n . Since particles are randomly selected, the resultant density contrast $\delta^{\text{sub}}(\mathbf{x})$ is unbiased and only differs from the underlying dark

matter field $\delta^{\text{mat}}(\mathbf{x})$ by a shot noise contribution

$$N_{\delta}(\mathbf{x}) = \delta^{\text{sub}}(\mathbf{x}) - \delta^{\text{mat}}(\mathbf{x}). \quad (11)$$

With multiple realizations of subsampling, we have checked that the average power spectra of these shot noise fields $N_{\delta}(\mathbf{x})$ are consistent with the theoretical value of $1/n$, where n is the number density of the subsample, with one caveat that the DTFE tessellation¹⁰ would introduce an extra smearing window function (Chan & Hamaus 2021).

To examine how reconstruction affects the shot noise, we can define a similar ‘‘shot noise’’ field $N_{\text{rec}}(\mathbf{x})$ after the reconstruction

$$N_{\text{rec}}(\mathbf{x}) = \delta_{\text{rec}}^{\text{sub}}(\mathbf{x}) - \delta_{\text{rec}}^{\text{mat}}(\mathbf{x}). \quad (12)$$

Here $\delta_{\text{rec}}^{\text{sub}}(\mathbf{x})$ and $\delta_{\text{rec}}^{\text{mat}}(\mathbf{x})$ are the reconstructed fields of the subsample $\delta^{\text{sub}}(\mathbf{x})$ and matter $\delta^{\text{mat}}(\mathbf{x})$ respectively. In Figure 4, we show the power spectra ratio $f^{\text{SN}}(k)$ between these two shot noise contributions

$$f^{\text{SN}}(k) = \frac{P_{\text{rec}}^{\text{SN}}}{P_{\delta}^{\text{SN}}}(k) = \frac{\langle N_{\text{rec}} N_{\text{rec}} \rangle}{\langle N_{\delta} N_{\delta} \rangle}(k). \quad (13)$$

In principle, an ensemble average of multiple subsamples $\langle f^{\text{SN}}(k) \rangle_s$ would be preferred. However, due to the numerical cost of the reconstruction, we only utilize one subsample for each situation. The results are reasonably stable and smooth and are adequate for our purpose. As shown, the reconstruction slightly increases the shot noise power before eventually dropping to zero at high- k . This small-scale damping is mainly

¹⁰ The density fields are estimated with the Delaunay tessellation (DTFE) method (Bernardeau & van de Weygaert 1996; Schaap & van de Weygaert 2000) to ensure the numerical stability of our reconstruction algorithm (Wang et al. 2017; Yu et al. 2017; Zhu et al. 2017).

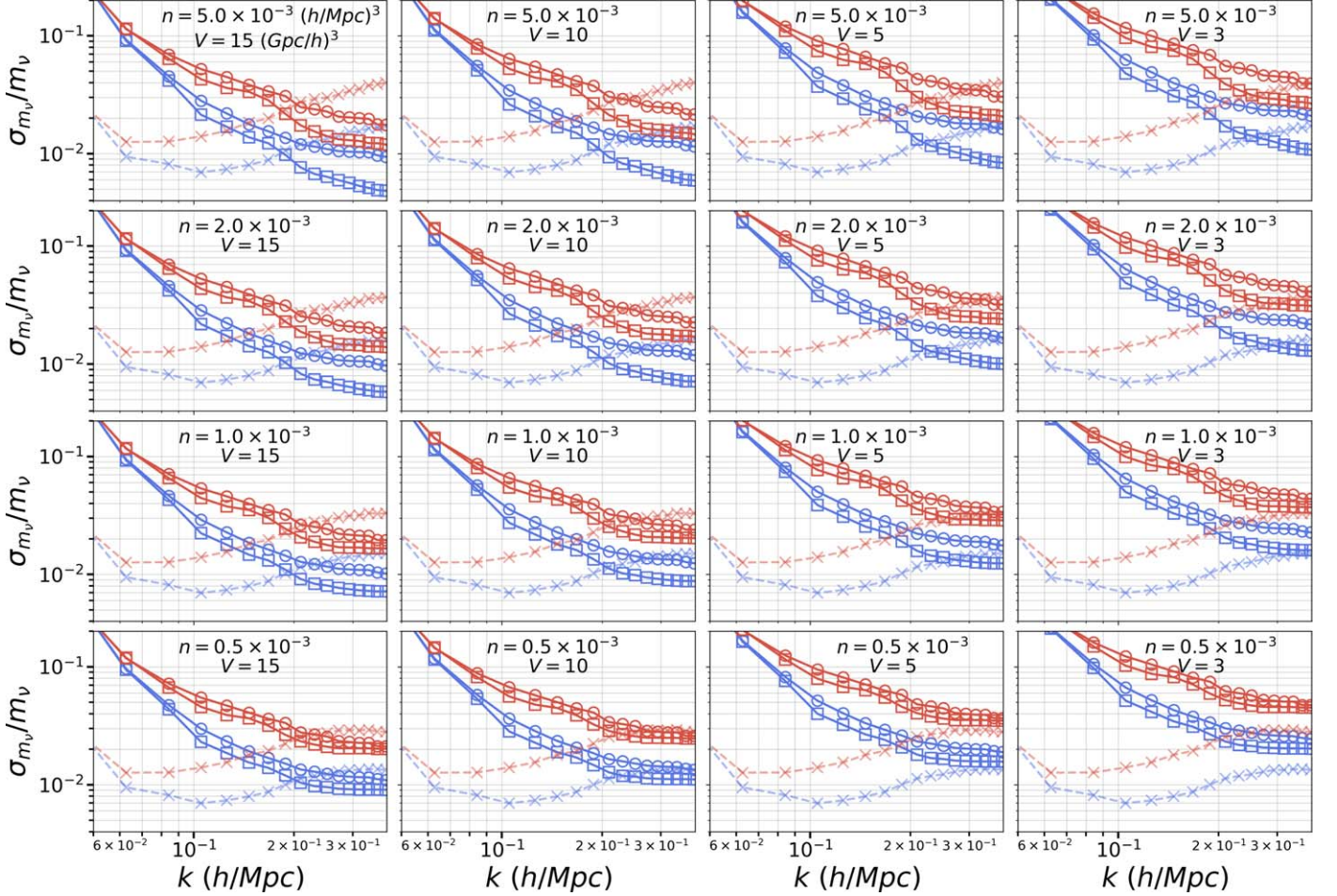


Figure 5. The constraints on neutrino mass Σm_ν for various survey parameters. The statistical errors are shown in solid lines and systematic bias in dashed lines. Different colors represent two different fiducial neutrino masses, red lines for $\Sigma m_\nu = 3 \times 50$ meV and blue lines for $\Sigma m_\nu = 3 \times 100$ meV. The units of the number density n and volume V are $(\text{Mpc}/h)^{-3}$ and $(\text{Gpc}/h)^3$ respectively.

caused by an internal smoothing process in our reconstruction algorithm (Wang et al. 2017; Zhu et al. 2017) to ensure numerical stability, and the physical damping scale k_{damp} is determined by the grid size.

Due to the computational cost of high-resolution reconstruction, our numerical test does not fully extend to much smaller scales before reaching the internal damping scale. However, compared to our forecasting results in Figures 5 and 6, i.e., those with the shot noise contribution, where most curves stabilize around $k = 0.3 \sim 0.4 h/\text{Mpc}$, we believe that, for our purpose, it is reasonable to assume the reconstruction algorithm does not significantly change the shot noise contribution.

With such an assumption, we could construct the covariance matrix of the biased tracer with the matter covariance matrix (Figure 1). Instead of rescaling the diagonal to Equation (8), we add the on-diagonal Poisson contribution

$$C_{\alpha\beta}^{\text{G}} = \frac{2k_F^3}{V_s(k)} \left(P(k_\alpha) + \frac{1}{n} \right)^2 \delta_{\alpha\beta}, \quad (14)$$

as well. Furthermore, following Chan & Blot (2017), we also include the non-Gaussian shot noise up to the $1/n^2$ order.

$$\begin{aligned} C_{\alpha\beta}^{\text{NG-SN}} &= \frac{k_F^3}{(2\pi)^3} \left[\frac{1}{n^3} + \frac{1}{n^2} (P(k_\alpha) + P(k_\beta)) \right. \\ &\quad \left. + \frac{2}{n^2} \int_{k_\alpha} \frac{d^3 p}{V_s(k_\alpha)} \right. \\ &\quad \left. \times \int_{k_\beta} \frac{d^3 p'}{V_s(k_\beta)} P_h(|\mathbf{p} + \mathbf{p}'|) \right] \end{aligned} \quad (15)$$

Meanwhile, we estimate large-scale bias using the halo model. Considering a sample of galaxies more luminous than a threshold luminosity L_{th} , the bias is expressed as

$$b_g = \frac{1}{n_g} \int_0^\infty b(m) \langle N(m, >L_{\text{th}}) \rangle \frac{dn}{dm} dm, \quad (16)$$

and the average number density n_g

$$n_g = \int_0^\infty \langle N(m, >L_{\text{th}}) \rangle \frac{dn}{dm} dm. \quad (17)$$

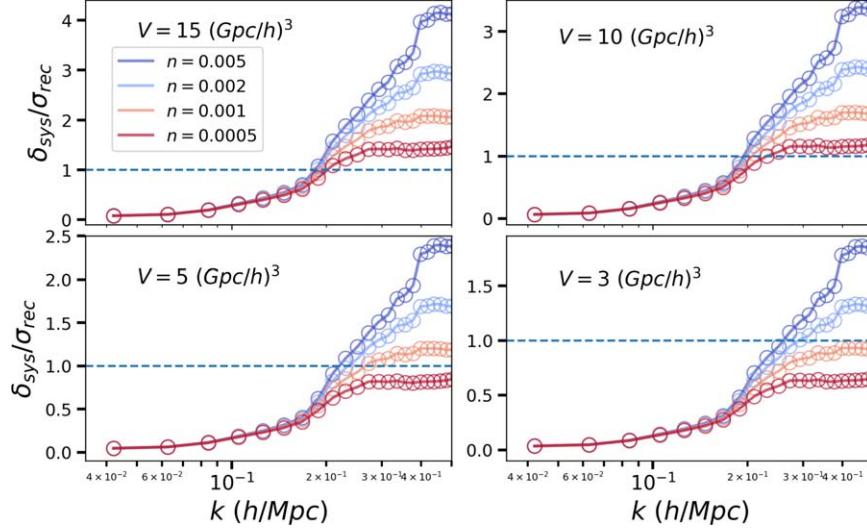


Figure 6. The ratio between systematic error and statistical uncertainty after the reconstruction. Here we only plot the fiducial neutrino mass $M_\nu = 3 \times 100$ meV, however, the result is numerically very similar for $M_\nu = 3 \times 50$ meV as well. As shown, we can safely ignore the reconstruction error before $k \lesssim 0.2$ h/Mpc for almost all cases here. For a low number density $n \sim 5 \times 10^{-4}$ medium-size survey $V \lesssim 5$ (Gpc/h) 3 , this is true in all relevant scales.

Here dn/dm is the halo mass function, $b(m)$ is the halo bias factor and $\langle N(m, >L_{\text{th}}) \rangle$ represents the halo occupation distribution (HOD) function for galaxies above luminosity L_{th} in halos of mass m . For our purpose, we adopt the HOD functions with varying luminosity thresholds L_{th} from Zehavi et al. (2005) and then estimate the bias of given number density n_g by matching the interpolated b_g - n_g relation. At redshift $z=0$, the obtained biases are: $b_g = 1.15, 1.31, 1.45, 1.66$ for number density $n_g = 5 \times 10^{-3}, 2 \times 10^{-3}, 10^{-3}, 5 \times 10^{-4}$ (Mpc/h) $^{-3}$ respectively.

In Figure 5, we present the final Fisher constraints (solid lines) of the neutrino mass Σm_ν , as well as its systematic errors (dashed lines) as a function of maximum wavenumber k_{max} . Each panel corresponds to a specific galaxy survey with number density n (ranging from 5×10^{-4} to 5×10^{-3} (h/Mpc) 3) and the survey volume V (from 3 to 15 (Gpc/h) 3). We can see that the reconstruction improvement is very sensitive to the shot noise contribution, which is consistent with the conclusion from the BAO reconstruction (Yu et al. 2017). Since, without the supersample effect, the covariance matrix scales with the survey volume $1/V$, via k_F^3 , this reconstruction improvement does not depend on V . For a survey with $n = 5 \times 10^{-4}$ (Mpc/h) $^{-3}$, the reconstruction will reduce the measurement error by roughly 20% \sim 30% at $k_{\text{max}} \sim 0.2$ h/Mpc for both fiducial neutrino masses. Clearly, higher number density will lead to much better constraints. For example, a survey with $n = 10^{-3}$ (Mpc/h) $^{-3}$ will improve the accuracy by $\sim 50\%$.

In Figure 6, we also plot the ratio between the systematic and statistical errors. As shown, in almost all cases here, we are free from reconstruction noise before $k_{\text{max}} \lesssim 0.2$ (h/Mpc). For medium-size surveys, e.g., $V \lesssim 5$ (Gpc/h) 3 , $n \lesssim 5 \times$

10^{-4} (Mpc/h) $^{-3}$, this is true at all relevant scales. On the other hand, for a Dark Energy Spectroscopic Instrument (DESI)-like survey ($n \sim 5 \times 10^{-4}$ (h/Mpc) 3 , $V \sim 10$ (Gpc/h) 3), the systematic error becomes comparable to the statistical error around $k \sim 0.25$ h/Mpc.

5. Discussion and Conclusion

In this paper, we investigate the possibility of utilizing the BAO reconstruction algorithm to detect the broadband signature, mainly focusing on the free-streaming scale caused by non-zero neutrino mass Σm_ν . Of course, the discussion in this paper could also apply for other broadband signatures, e.g., modified gravity. Due to the Gaussianization of the reconstruction, the reconstruction could potentially improve the measurement accuracy of neutrino mass. Even though there are difficulties in theoretical modeling of the reconstruction output, one could still calibrate and measure from simulation. With the Fisher matrix, we showed that the reconstruction could reduce the constraint by roughly a factor of two. Given the intrinsic numerical variation of the algorithm, we further examined the potential systematic bias and demonstrated that this type of randomness could be important for a DESI-like survey.

As an initial investigation, more challenges need to be examined, most crucially the nonlinear clustering bias and redshift-space distortion. As demonstrated in Yu et al. (2017); Wang & Pen (2019) and Zhu et al. (2018), they will certainly decrease the information gain from the reconstruction. Furthermore, there are a variety of systematic uncertainties one needs to consider as well, including, e.g., different

resolutions, cosmological parameters, tracer density, etc. We will defer these uncertainties to future investigations.

Acknowledgments

X.W. would like to thank the support from the science research grants from the China Manned Space Project with NO. CMS-CSST-2021-B01. D.I. was supported by the World Premier International Research Center Initiative (WPI), MEXT, Japan. U.L. receives support from the Ontario Research Fund: Research Excellence Program (ORF-RE), Natural Sciences and Engineering Research Council of Canada (NSERC) [funding reference number RGPIN-2019-067, CRD 523638-201, 555585-20], Canadian Institute for Advanced Research (CIFAR), Canadian Foundation for Innovation (CFI), the National Natural Science Foundation of China (NSFC, Grant No. 11929301), Simons Foundation, Thoth Technology Inc, and Alexander von Humboldt Foundation. Computations were performed on the Niagara supercomputers at the SciNet HPC Consortium. SciNet is funded by: the Canada Foundation for Innovation; the Government of Ontario; Ontario Research Fund—Research Excellence; and the University of Toronto.

ORCID iDs

Derek Inman  <https://orcid.org/0000-0001-6039-9058>

Xin Wang  <https://orcid.org/0000-0002-2472-6485>

Ue-Li Pen  <https://orcid.org/0000-0003-2155-9578>

References

- Alam, S., Ata, M., Bailey, S., et al. 2017, *MNRAS*, 470, 2617
- Bayer, A. E., Banerjee, A., & Seljak, U. 2022, *PhRvD*, 105, 123510
- Bernardeau, F., & van de Weygaert, R. 1996, *MNRAS*, 279, 693
- Blake, C., & Glazebrook, K. 2003, *ApJ*, 594, 665
- Bond, J. R., & Efstathiou, G. 1987, *MNRAS*, 226, 655
- Brandbyge, J., Hannestad, S., Haugbølle, T., & Wong, Y. Y. Y. 2010, *JCAP*, 2010, 014
- Chan, K. C., & Blot, L. 2017, *PhRvD*, 96, 023528
- Chan, K. C., & Hamaus, N. 2021, *PhRvD*, 103, 043502
- Chen, X., Dvorkin, C., Huang, Z., Namjoo, M. H., & Verde, L. 2016, *JCAP*, 2016, 014
- Clifton, T., Ferreira, P. G., Padilla, A., & Skordis, C. 2012, *PhR*, 513, 1
- Desjacques, V., Jeong, D., & Schmidt, F. 2018, *PhR*, 733, 1
- Eisenstein, D. 2002, in ASP Conf. Ser. 280, Next Generation Wide-Field Multi-Object Spectroscopy, ed. M. J. I. Brown & A. Dey (San Francisco, CA: ASP), 35
- Eisenstein, D. J., Seo, H.-J., Sirko, E., & Spergel, D. N. 2007, *ApJ*, 664, 675
- Giannantonio, T., Martinelli, M., Silvestri, A., & Melchiorri, A. 2010, *JCAP*, 2010, 030
- Hada, R., & Eisenstein, D. J. 2018, *MNRAS*, 478, 1866
- Harnois-Déraps, J., Pen, U.-L., Iliev, I. T., et al. 2013, *MNRAS*, 436, 540
- Hu, W., & Haiman, Z. 2003, *PhRvD*, 68, 063004
- Hu, W., & Sugiyama, N. 1996, *ApJ*, 471, 542
- Huterer, D., & Takada, M. 2005, *Aph*, 23, 369
- Huterer, D., Takada, M., Bernstein, G., & Jain, B. 2006, *MNRAS*, 366, 101
- Inman, D., Emberson, J. D., Pen, U.-L., et al. 2015, *PhRvD*, 92, 023502
- Ivanov, M. M., Simonović, M., & Zaldarriaga, M. 2020, *PhRvD*, 101, 083504
- Jing, Y. P., Zhang, P., Lin, W. P., Gao, L., & Springel, V. 2006, *ApJL*, 640, L119
- Kitaura, F. S., & EnBlin, T. A. 2008, *MNRAS*, 389, 497
- Lesgourgues, J., & Pastor, S. 2006, *PhR*, 429, 307
- Li, J., & Zhao, G.-B. 2019, *ApJ*, 871, 196
- Li, Y., Zhu, H.-M., & Li, B. 2021, arXiv:2102.09007
- Mangano, G., Miele, G., Pastor, S., et al. 2005, *NuPhB*, 729, 221
- Neyrinck, M. C. 2011, *ApJ*, 742, 91
- Ota, A., Seo, H.-J., Saito, S., & Beutler, F. 2021, *PhRvD*, 104, 123508
- Palanque-Delabrouille, N., Yèche, C., Schöneberg, N., et al. 2020, *JCAP*, 2020, 038
- Pan, Q., Pen, U.-L., Inman, D., & Yu, H.-R. 2016, arXiv:1611.10013
- Pan, Q., Pen, U.-L., Inman, D., & Yu, H.-R. 2017, *MNRAS*, 469, 1968
- Peebles, P. J. E., & Yu, J. T. 1970, *ApJ*, 162, 815
- Planck Collaboration, Aghanim, N., Akrami, Y., et al. 2020, *A&A*, 641, A6
- Riemer-Sørensen, S., Blake, C., Parkinson, D., et al. 2013, *ApJ*, 763, 89
- Rimes, C. D., & Hamilton, A. J. S. 2005, *MNRAS*, 360, L82
- Rimes, C. D., & Hamilton, A. J. S. 2006, *MNRAS*, 371, 1205
- Rudd, D. H., Zentner, A. R., & Kravtsov, A. V. 2008, *ApJ*, 672, 19
- Schaap, W. E., & van de Weygaert, R. 2000, *A&A*, 363, L29
- Schmidt, F., Elsner, F., Jasche, J., Nguyen, N. M., & Lavaux, G. 2019, *JCAP*, 2019, 042
- Schmittfull, M., Baldauf, T., & Zaldarriaga, M. 2017, *PhRvD*, 96, 023505
- Seljak, U., Aslanyan, G., Feng, Y., & Modi, C. 2017, *JCAP*, 2017, 009
- Seo, H., & Eisenstein, D. J. 2003, *ApJ*, 598, 720
- Shi, Y., Cautun, M., & Li, B. 2018, *PhRvD*, 97, 023505
- Sunyaev, R. A., & Zeldovich, Y. B. 1970, *Ap&SS*, 7, 3
- Tegmark, M., Eisenstein, D. J., Strauss, M. A., et al. 2006, *PhRvD*, 74, 123507
- Villaescusa-Navarro, F., Bird, S., Peña-Garay, C., & Viel, M. 2013, *JCAP*, 2013, 019
- Wang, X., & Pen, U.-L. 2019, *ApJ*, 870, 116
- Wang, X., Yu, H.-R., Zhu, H.-M., et al. 2017, *ApJL*, 841, L29
- Weinberg, D. H. 1992, *MNRAS*, 254, 315
- Yu, Y., Zhu, H.-M., & Pen, U.-L. 2017, *ApJ*, 847, 110
- Zehavi, I., Zheng, Z., Weinberg, D. H., et al. 2005, *ApJ*, 630, 1
- Zhu, H.-M., Yu, Y., & Pen, U.-L. 2018, *PhRvD*, 97, 043502
- Zhu, H.-M., Yu, Y., Pen, U.-L., Chen, X., & Yu, H.-R. 2017, *PhRvD*, 96, 123502